Since January 2020 Elsevier has created a COVID-19 resource centre with free information in English and Mandarin on the novel coronavirus COVID-19. The COVID-19 resource centre is hosted on Elsevier Connect, the company's public news and information website.

European Journal of Medicinal Chemistry 240 (2022) 114570

Contents lists available at ScienceDirect

European Journal of Medicinal Chemistry

journal homepage: www.elsevier.com/locate/ejmech

A multi-pronged evaluation of aldehyde-based tripeptidyl main protease inhibitors as SARS-CoV-2 antivirals

Yuying Ma [a,1], Kai S. Yang [a,1], Zhi Zachary Geng [a,1], Yugendar R. Alugubelli [a,1], Namir Shaabani [b,1], Erol C. Vatansever [a,1], Xinyu R. Ma [a,1], Chia-Chuan Cho [a,1], Kaustav Khatua [a,1], Jing Xiao [a], Lauren R. Blankenship [a], Ge Yu [a], Banumathi Sankaran [c], Pingwei Li [d], Robert Allen [b], Henry Ji [b,**], Shiqing Xu [a,***], Wenshe Ray Liu [a,d,e,f,*]

[a] Texas A&M Drug Discovery Laboratory, Department of Chemistry, Texas A&M University, College Station, TX, 77843, USA
[b] Sorrento Therapeutics, Inc. San Diego, CA, 92121, USA
[c] Molecular Biophysics and Integrated Bioimaging, Berkeley Center for Structural Biology, Laurence Berkeley National Laboratory, Berkeley, CA, 94720, USA
[d] Department of Biochemistry and Biophysics, Texas A&M University, College Station, TX, 77843, USA
[e] Institute of Biosciences and Technology and Department of Translational Medical Sciences, College of Medicine, Texas A&M University, Houston, TX, 77030, USA
[f] Department of Molecular and Cellular Medicine, College of Medicine, Texas A&M University, College Station, TX, 77843, USA

ARTICLE INFO

Keywords:
COVID-19
SARS-CoV-2
Main protease
Covalent inhibitors
Tripeptides

ABSTRACT

As an essential enzyme of SARS-CoV-2, the COVID-19 pathogen, main protease (M^{Pro}) is a viable target to develop antivirals for the treatment of COVID-19. By varying chemical compositions at both P2 and P3 positions and the *N*-terminal protection group, we synthesized 18 tripeptidyl M^{Pro} inhibitors that contained also an aldehyde warhead and β-(S-2-oxopyrrolidin-3-yl)-alaninal at the P1 position. Systematic characterizations of these inhibitors were conducted, including their *in vitro* enzymatic inhibition potency, X-ray crystal structures of their complexes with M^{Pro}, their inhibition of M^{Pro} transiently expressed in 293T cells, and cellular toxicity and SARS-CoV-2 antiviral potency of selected inhibitors. These inhibitors have a large variation of determined *in vitro* enzymatic inhibition IC_{50} values that range from 4.8 to 650 nM. The determined *in vitro* enzymatic inhibition IC_{50} values reveal that relatively small side chains at both P2 and P3 positions are favorable for achieving high *in vitro* M^{Pro} inhibition potency, the P3 position is tolerable toward unnatural amino acids with two alkyl substituents on the α-carbon, and the inhibition potency is sensitive toward the *N*-terminal protection group. X-ray crystal structures of M^{Pro} bound with 16 inhibitors were determined. In all structures, the M^{Pro} active site cysteine interacts covalently with the aldehyde warhead of the bound inhibitor to form a hemithioacetal that takes an *S* configuration. For all inhibitors, election density around the *N*-terminal protection group is weak indicating possible flexible binding of this group to M^{Pro}. In M^{Pro}, large structural variations were observed on residues N142 and Q189. Unlike their high *in vitro* enzymatic inhibition potency, most inhibitors showed low potency to inhibit M^{Pro} that was transiently expressed in 293T cells. Inhibitors that showed high potency to inhibit M^{Pro} transiently expressed in 293T cells all contain *O-tert*-butyl-threonine at the P3 position. These inhibitors also exhibited relatively low cytotoxicity and high antiviral potency. Overall, our current and previous studies indicate that *O-tert*-butyl-threonine at the P3 site is a key component to achieve high cellular and antiviral potency for tripeptidyl aldehyde inhibitors of M^{Pro}.

Abbreviations: COVID-19, coronavirus disease 2019; SARS-CoV-2, severe acute respiratory syndrome coronavirus 2; MPro, main Protease; MPI, main Protease Inhibitor; SAR, structure-activity relationship; eGFP, enhanced green fluorescent protein; CBZ, benzyloxycarbonyl.

* Corresponding author. Texas A&M Drug Discovery Laboratory, Department of Chemistry, Texas A&M University, College Station, TX, 77843, USA
** Corresponding author. ,
*** Corresponding author.
E-mail addresses: hji@sorrentotherapeutics.com (H. Ji), shiqing.xu@tamu.edu (S. Xu), wsliu2007@tamu.edu (W.R. Liu).

[1] Contributed equally to the paper.

https://doi.org/10.1016/j.ejmech.2022.114570
Received 17 May 2022; Received in revised form 22 June 2022; Accepted 23 June 2022
Available online 27 June 2022

1. Introduction

COVID-19 is the current prevailing pandemic that has devastated much of the world. As the COVID-19 pathogen, SARS-CoV-2 uses its membrane Spike protein to recognize the human receptor ACE2 for infection [1,2]. Current COVID-19 vaccines all target this process for the neutralization of the virus. However, the continuous emergence of new viral strains that evade vaccines demands other antivirals to be developed as well. The genome of SARS-CoV-2 encodes a large open reading frame ORF1ab that is translated to two large polypeptides pp1a and pp1b in the human cell host [3,4]. The processing of pp1a and pp1b to 16 nonstructural proteins (nsps) that are functionally critical to the viral replication relies on proteolytic activities of two internal nsp fragments, nsp3 and nsp5 [5]. Nsp5 is also called 3C-like protease and more recently main protease (M^{Pro}). Since M^{Pro} hydrolyzes 13 out of the total of 16 nsps, it has been considered as a viable target for the development of antivirals. In the past year, a number of papers have been published on the development of peptidyl aldehydes that contain β-(S-2-oxopyrrolidin-3-yl)-alaninal (opal) at the P1 position as potent M^{Pro} inhibitors [6–14]. Other inhibitors were developed as well including nirmatrelvir that has been approved by the U.S. Food and Drug Administration for its combined use with ritonavir as a therapy, branded as paxlovid, for COVID-19 and S-217622 that is undergoing clinical trials for COVID-19 in Japan [15–30]. However, systematic structure-activity relationship (SAR) studies of opal-based M^{Pro} inhibitors are needed. In the current study, we explore variations at the P2 and P3 positions and the *N*-terminal protection group in opal-based tripeptidyl M^{Pro} inhibitors. Our study indicates that *O-tert*-butyl-threonine at the P3 position in an opal-based M^{Pro} inhibitor is critical for achieving high potency inhibiting M^{Pro} expressed in human host cells and antiviral potency against SARS-CoV-2.

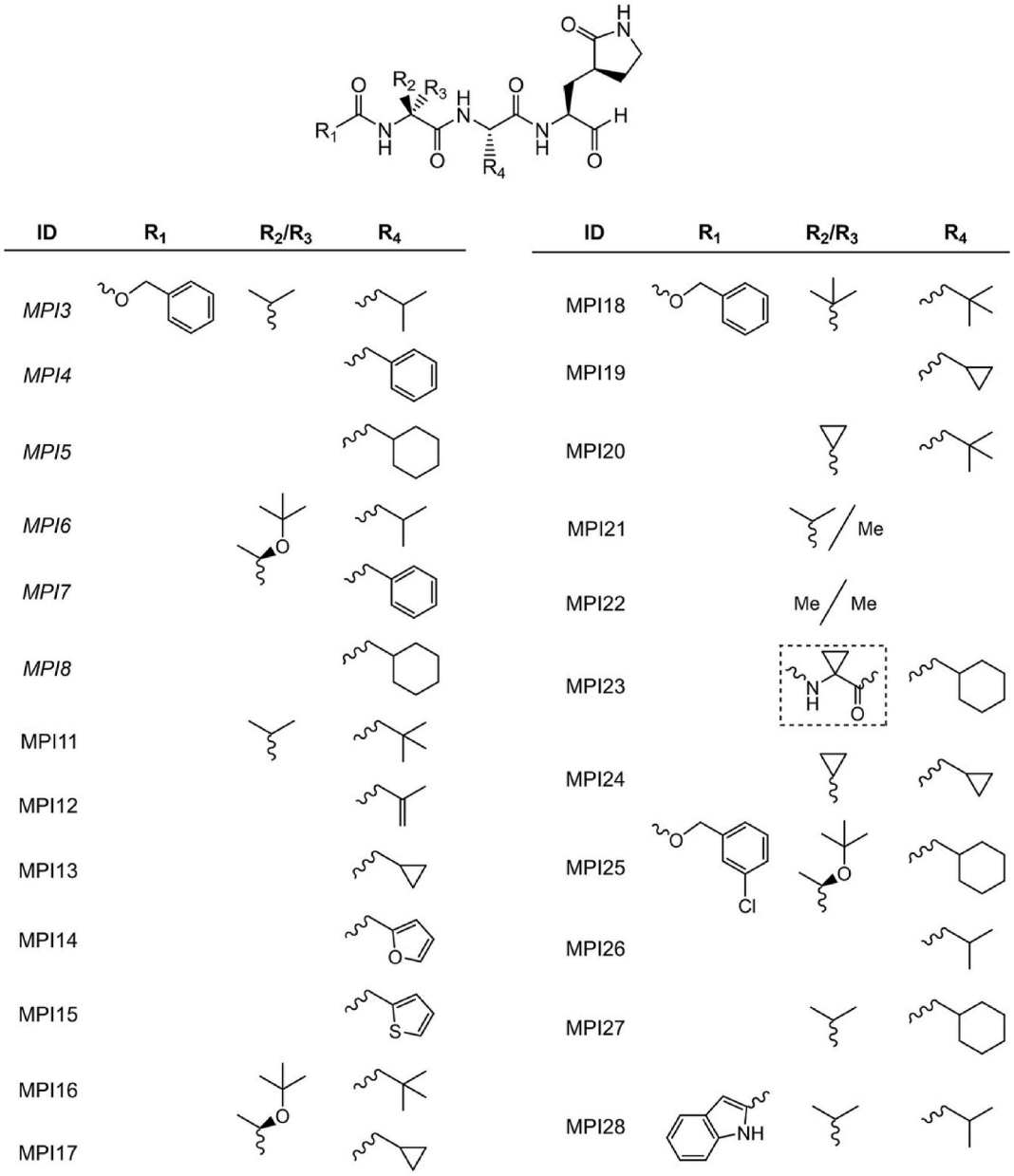

Fig. 1. Structures of tripeptidyl M^{Pro} inhibitors **MPI11–28**. Inhibitors that have just a single component at R_2/R_3 shown contain a hydrogen at the R_3 position. **MPI3-8** were previously developed and are shown for comparison.

2. Results

2.1. The design and synthesis of MPI11-28

In previous studies, we developed MPI1-10 and characterized both their M^{Pro} inhibition potency and their antiviral potency [13,14]. As a tripeptidyl aldehyde, MPI8 shows the highest antiviral potency with an EC_{50} value of 30 nM to neutralize SARS-CoV-2 (USA-WA1/2020) in Vero E6 cells [31]. MPI3, another tripeptidyl aldehyde, doesn't have high antiviral potency. However, it has the highest *in vitro* M^{Pro} inhibition potency with an IC_{50} value of 8.5 nM [13]. To explore how substituents at different positions in a tripeptidyl opal-based M^{Pro} inhibitor (Fig. 1) influence its potency, we decided to carry out a systematic structure-activity relationship (SAR) study. We maintained opal at the P1 position due to its established preferential binding to the M^{Pro} P1 binding pocket and its ability to form a covalent adduct with C145, the M^{Pro} catalytic cysteine. M^{Pro} tolerates leucine and phenylalanine at the P2 position in a substrate. Therefore, we chose to vary this site in our inhibitor design among β-alkyl alanines with sizes between or around leucine and phenylalanine. Chosen alkyl substituents include isopropyl, phenyl, cyclohexyl, *t*-butyl, isopropenyl, cyclopropyl, 2-furyl, and 2-thienyl. M^{Pro} doesn't have a binding pocket for the P3 position in a substrate. However, native M^{Pro} substrates have valine or a similar size residue at this position. Based on known opal inhibitors and substrates of M^{Pro}, we varied this site among amino acids including valine, *O-tert*-butyl-threonine, L-cyclopropylglycine, *L-tert*-butyl-glycine, L-α-methyl-valine, dimethylglycine, and 1-aminocyclopropane-1-carboxylate. The *N*-terminal protection group was chosen among benzyloxycarbonyl (CBZ), *m*-chloro CBZ, and indole-2-carboxylate due to their demonstrated contributions to antiviral potency [6,10]. A total of 18 new M^{Pro} inhibitors, designated as MPI11-28 shown in Fig. 1, were designed. We synthesized all inhibitors according to the synthetic route shown in Scheme 1. In this synthesis, a P2 amino acid ester was conjugated with a *N*-protected P3 amino acid and the afforded product was then hydrolyzed to free its *C*-terminal carboxylate for a reaction with β-(S-2-oxopyrrolidin-3-yl)-alanine ester. An obtained tripeptidyl ester was reduced to afford a *C*-terminal alcohol that was then oxidized via Dess-Martin oxidation in a mild condition to make a final product.

2.2. Kinetic characterizations of MPI11-28 on their enzymatic inhibition of M^{Pro}

We followed a previously established protocol that uses Sub3 (Dabcyl-KTSAVLQSGFRKME-Edans), a fluorogenic peptide substrate of M^{Pro} to determine IC_{50} values for MPI11-28 [28]. In this assay, we preincubated M^{Pro} with an inhibitor for 30 min before Sub3 was added and the fluorescent product formation (Ex: 336 nm/Em: 455 nm) was recorded in a fluorescence plate reader. 30 min incubation time with M^{Pro} is a standard procedure that has been used by multiple labs in the determination of IC_{50} values for M^{Pro} inhibitors [11,27,28,32]. Since MPI11-28 are reversible covalent inhibitors, their incubation times with M^{Pro} are not expected to significantly influence their determined IC_{50} values. Tests involving MPI11 in three different incubation times, 15, 30, and 60 min, led to very similar determined IC_{50} values (Supplementary Fig. 1). Except MPI15 that is insoluble in DMSO and therefore was not characterized, all other inhibitors displayed well traceable inhibition curves as shown in Fig. 2. We fit all data to a four-parameter variable slope inhibition equation in GraphPad 9.0 to obtain IC_{50} values for all inhibitors. As shown in Table 1, MPI11-28 display a large variation of IC_{50} values that ranges from 4.8 to 650 nM. MPI11-14 all contain valine at the P3 position. They are among the most *in vitro* potent inhibitors for M^{Pro}. MPI13-14 have determined IC_{50} values around 5 nM. Since 10 nM M^{Pro} is the lowest enzyme concentration we can use to do the inhibition analysis, 5 nM is technically the lowest IC_{50} value we can detect. Therefore, M^{Pro} inhibition potency for MPI13-14 is likely higher than the numbers shown in Table 1. In comparison to MPI13-14, MPI11-12 have slightly higher IC_{50} values. In previous work, we developed another three M^{Pro} inhibitors MPI3-5 that also contain a valine at the P3 site. All three have low IC_{50} values. All 7 inhibitors that have valine at the P3 position and a *N*-terminal CBZ protection group are among the most potent M^{Pro} inhibitors *in vitro*. A P3 valine apparently favors the enzyme inhibition kinetics. A comparison of all seven inhibitors also reveals that a residue at the P2 position with a size close to leucine leads to better M^{Pro} inhibition. β−Cyclopropyl alanine and β-(furan-2yl) alanine that have a more rigid side chain than leucine favor the enzyme inhibition kinetics more. MPI6-8 that have a P3 *O-tert*-butyl-threonine were developed previously and showed high antiviral potency. We synthesized two more M^{Pro} inhibitors with a P3 *O-tert*-butyl-threonine, MPI16-17. Both have an IC_{50} value similar to MPI6-8. Varying the P2 position does not seem to significantly change *in vitro* M^{Pro} inhibition potency among this group of inhibitors. To explore further on whether variations at the P3 position lead to different inhibition potency, we developed MPI18-24. Variants include two dialkyl glycines and 1-aminocyclopropane-1-carboxylate that are not standard L-amino acids. Except MPI23 that contains a P3 1-aminocyclopropane-1-carboxylate, all other inhibitors have an IC_{50} value below 100 nM. The more rigid P3 position in MPI23 likely contributes to its less favorable M^{Pro} inhibition kinetics. MPI24 is structurally similar to MPI13. Its enzyme inhibition potency is similar to MPI13 as well. Three inhibitors MPI25-27 that have a *N*-terminal *m*-chloro CBZ group were developed and characterized as well. In comparison to their regular CBZ-containing counterpart inhibitors MPI8, MPI6, and MPI5, they display more than 5-fold higher IC_{50} values. Apparently adding an *m*-chloro substituent to the terminal CBZ group doesn't improve *in vitro*

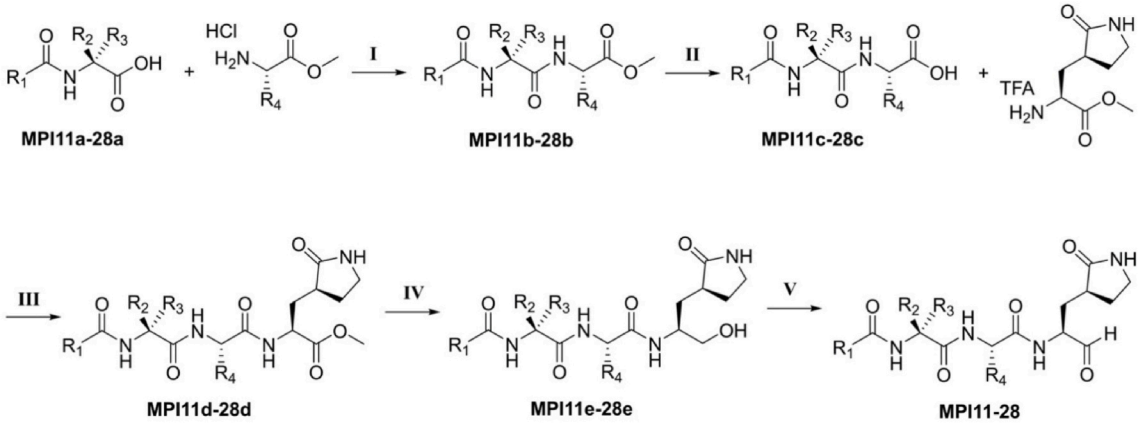

Scheme 1. Reagents and conditions: (I) HATU, DIPEA, DMF; (II) $LiOH{\bullet}H_2O$, THF/H_2O; (III) HATU, DIPEA, DMP; (IV) $LiBH_4$, THF; (V) DMP, DCM.

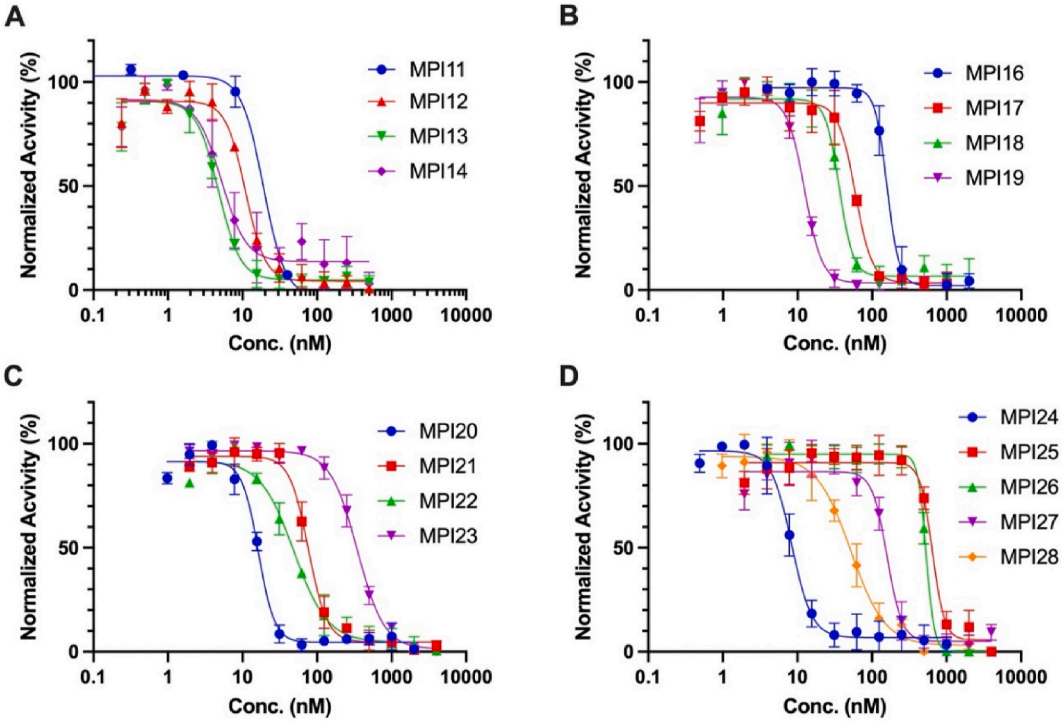

Fig. 2. Inhibition curves of MPI11-28 on M^{Pro}. Triplicate experiments were performed for each compound. For all experiments, 20 or 10 nM M^{Pro} was incubated with an inhibitor for 30 min before 10 μM Sub3 was added. The M^{Pro}-catalyzed Sub3 hydrolysis rate was determined by measuring linear increase of product fluorescence (Ex: 336 nm/Em: 455 nm) for 5 min.

Table 1
Determined enzymatic IC_{50} and cellular EC_{50} values of M^{Pro} inhibitors.

ID	Enzymatic IC_{50} (nM)	Cellular EC_{50} (μM)	Antiviral EC_{50} (μM)	CC_{50} (μM)	PDB Entry	ID	Enzymatic IC_{50} (nM)	Cellular EC_{50} (μM)	Antiviral EC_{50} (μM)	CC_{50} (μM)	PDB Entry
MPI3	*8.5* [b]	*> 2* [c]			*7JQ0*	MPI18	36	0.86	>5[e]/0.71[f]/>5[g]	>200	7RVR
MPI4	*15* [b]	*> 2* [c]			*7JQ1*	MPI19	13	1.5			7RVS
MPI5	*33* [b]	*0.66* [c]			*7JQ2*	MPI20	16	>2			7RVT
MPI6	*60* [b]	*0.12* [c]			*7JQ3*	MPI21	77	>2			7RVU
MPI7	*47* [b]	*0.19* [c]			*7JQ4*	MPI22	49	>10			7RVV
MPI8	*105* [b]	*0.03* [c]	*0.030* [e]	109.2	*7JQ5*	MPI23	350	>10			7RVW
MPI11	19	>2			7RVM	MPI24	8.4	>2			7RVX
MPI12	11	>2			7RVN	MPI25	650	0.14	2.2[e]/1.6[f]/0.87[g]	130.0	7RVY
MPI13	4.8[d]	>2			7RVO	MPI26	530	0.23	1.9[e]/0.65[f]/1.6[g]	182.9	7RVZ
MPI14	5.2[d]	>2			7RVP	MPI27	160	0.63	>5[e]/>5[f]/3.2[g]	114.0	7RW0
MPI15	n.d.[a]	n.d.[a]			–	MPI28	52	>10			7RW1
MPI16	150	0.056	1.2[e]/1.2[f]/0.58[g]	>200	7RVQ	nirmatrelvir [38]	66	3.4	1.30		
MPI17	60	0.097	1.2[e]/1.8[f]/1.1[g]	>200	–	GC376 [31]	30	>2	3.37		

[a] Its IC_{50} and EC_{50} values were not determined (n.d.) due to insolubility.
[b] Data were taken from Ref. [13].
[c] Data were taken from Refs. [31].
[d] Reaching the detection limit.
[e] Antiviral EC_{50} value for the USA-WA1/2020 strain.
[f] Antiviral EC_{50} value for the Beta strain.
[g] Antiviral EC_{50} value for the Delta strain.

enzyme inhibition potency. MPI28 has an *N*-terminal indole-2-carboxylate. In comparison to its CBZ counterpart inhibitor MPI3, MPI28 has a 6-folder higher IC_{50} value. In comparison to indole-2-carboxylate, it is evident that CBZ serves as a better *N*-terminal group for improved *in vitro* enzyme inhibition potency.

2.3. X-ray crystallography analysis of M^{Pro} bound with 16 different inhibitors

To characterize our developed inhibitors on their interactions with M^{Pro}, we crystallized M^{Pro} in its apo form, soaked apo-M^{Pro} crystals with different inhibitors and then determined structures of M^{Pro} bound with different inhibitors using X-ray crystallography. Among 17 inhibitors

that we used to soak crystals, 16 were observable in the active site of M^{Pro}. All structures were determined to high resolutions (Table S1). For all inhibitors, their calculated $2F_o$-F_c electron density maps in the M^{Pro} active site clearly show a covalent interaction with M^{Pro} C145 to generate a hemithioacetal (Fig. 3A). In all formed hemithioacetals, the hemithioacetal alcohol takes an *S* configuration. In most calculated structures, electron density around inhibitors have defined shapes for modeling the P1, P2 and P3 residues. For MPI12, the isopropenyl group has very weak electron density around its C1 and C3 atoms, indicating that the isopropenyl group is probably freely rotating around its C2 atom in the active site of M^{Pro}. For MPI26 and MPI28 that have a P2 leucine, electron density around the side chain isopropyl group is also weak, indicating its flexible conformations at the M^{Pro} active site. Although the *N*-terminal group of inhibitors including MPI11, MPI12, MPI18, and MPI19 were successfully modeled, most calculated structures have relatively weak electron density around the inhibitor *N*-terminal group, indicating weak binding of the *N*-terminal group at the active site.

In M^{Pro}-MPI11 as shown in Fig. 3B, MPI11 forms extensive hydrogen bonds with M^{Pro}. The hemithioacetal hydroxyl group is within the hydrogen bond distance to three backbone α-amines in residues 143–145 that form an oxyanion hole to facilitate the enzyme-catalyzed hydrolysis of a substrate. Due to the preferential binding of a negative charged hydroxyl group at this position, it is likely that the hemithioacetal hydroxy group is deprotonated to strongly interact with the three backbone α-amines, explaining the exclusive *S* configuration of the formed hemithioacetal. The opal side-chain lactam forms three hydrogen bonds with residues E166, N142, and F140 and its backbone α-amine forms a hydrogen bond with H164. The side chain of the P2 β-*tert*-butyl-alanine (4-methyl-leucine) is involved in van der Waals interactions with M^{Pro} residues including M49, H41, M165, D187, and

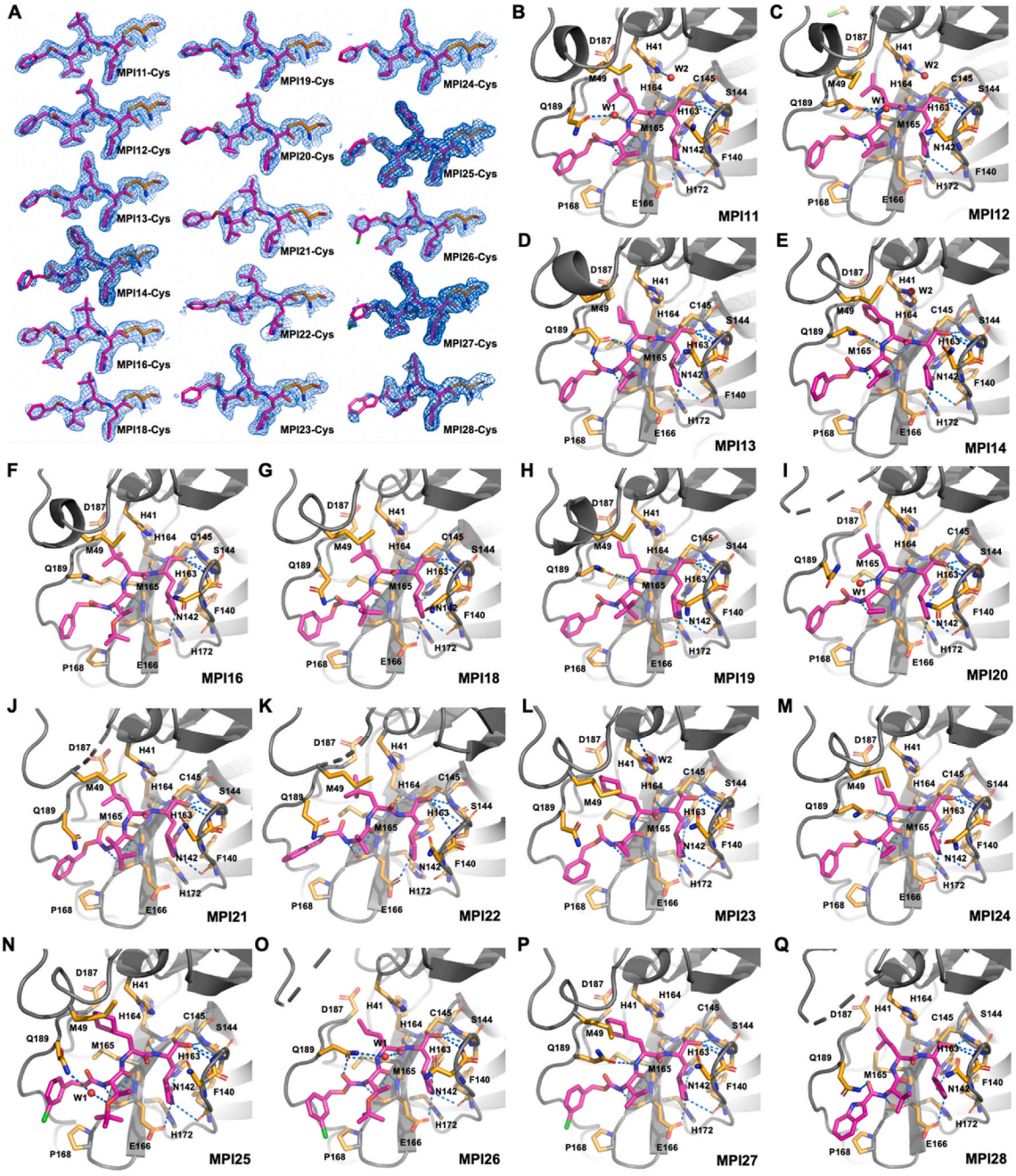

Fig. 3. Crystal structures of M^{Pro} bound with 16 MPIs. (A) Contoured $2F_o$-F_c maps at the 1σ level around 16 MPIs and C145 in the active site of M^{Pro}. (B–Q) Interactions between 16 MPIs and the M^{Pro} active site residues.

Q189. It is interesting to note that the M49-containing loop has weak electron density around it, indicating flexible conformations of this loop when MPI11 binds to the M^{Pro} active site. The MPI11 P2 α-amine interacts with the side chain of Q189 indirectly through two water-bridged hydrogen bonds. The M^{Pro}-MPI11 structure shows that the *tert*-butyl group is within a close van der Waals distance to the Q189-containing loop of M^{Pro}. To accommodate a chemical moiety bigger than β-*tert*-butyl-alanine, M^{Pro} will need to rearrange the Q189-containing loop to enlarge the P2 binding pocket. The P3 valine of MPI11 forms two hydrogen bonds with the backbone α-amine and α-carbonyl groups of E166. Its side chain forms van der Waals interactions with the side chain of E166. The *N*-terminal CBZ of MPI11 interacts hydrophobically with the backbone of the Q189-containing loop and the side chain of P168. However, its weak electron density indicates loose binding. In M^{Pro}-MPI11, the side chain of N142 flips away from the opal side chain of MPI11. The M^{Pro}-MPI12 structure around the active site is shown in Fig. 3C. MPI12 is involved in hydrogen bonding interactions with M^{Pro} mostly similar to MPI11. It forms an *S*-configuration thiohemiacetal covalent adduct with M^{Pro}. Unlike in the M^{Pro}-MPI11 structure, Q189 in M^{Pro}-MPI12 forms a hydrogen bond directly with the MPI12 P2 α-amine and interacts indirectly with the P2 α-carbonyl oxygen through a water-bridged hydrogen bond network. In M^{Pro}-MPI12, the P2 β-isopropenyl-alanine side chain doesn't have a fixed conformation. Additional modification to this side chain to introduce tighter binding to M^{Pro} is likely. In M^{Pro}-MPI12, N142 adopts a conformation that partially caps the P1 binding pocket in M^{Pro}. As in M^{Pro}-MPI11, the M49-containing loop has weak electron density around it. The M^{Pro}-MPI13 structure around the active site is shown in Fig. 3D. Interactions between MPI13 and M^{Pro} are mostly similar to that between MPI12 and M^{Pro}. N142 adopts a conformation like the one in M^{Pro}-MPI11. Unlike MPI12, the P2 cyclopropyl side chain of MPI13 has defined, strong electron density around it and interacts with the van der Waals distance with side chains from H41, D187 and Q189. This observation explains high *in vitro* enzymatic inhibition potency for inhibitors including MPI13, MPI19 and MPI24. MPI14 shown in Fig. 3E interacts with M^{Pro} mostly similar to MPI11. MPI14 has a P2 β-(2-furanyl)-alanine residue that has defined, strong electron density around the furan side chain. The furan group is in parallel with the H41 imidazole side chain so that the two aromatic groups are likely engaged in a π-π stacking interaction. This π-π stacking interaction likely contributes to the high *in vitro* enzymatic inhibitor potency of MPI14. In M^{Pro}-MPI14, Q189 has weak electron density around its side chain. It is not involved in hydrogen bonding interactions with MPI14 directly or indirectly. In both M^{Pro}-MPI13 and M^{Pro}-MPI14, the M49-containing loop has weak electron density.

MPI16 differs from MPI11 in its P3 position that is *O*-*tert*-butyl-threonine. As shown in Fig. 3F, MPI16 maintains most hydrogen bonding interactions that show in the M^{Pro}-MPI11 complex structure. The M^{Pro} Q189 side chain amide is 3.5 Å to the P2 α-amine of MPI16. This is around the borderline for a hydrogen bond interaction. In M^{Pro}-MPI16, the N142 side chain adopts a conformation that caps the MPI16 P1 opal side chain. Compared to MPI11, MPI16 has an additional P3 *O*-*tert*-butyl group. Its location can be clearly refined that shows van der Waals interactions with P168 and E166. MPI18 has a chemical structure very similar to MPI11 except at the P3 position that has an additional methyl group on the β-carbon. Its interactions with M^{Pro} as shown in Fig. 3G are also similar to that involving MPI11. Visible differences are at M^{Pro} residues N142 and Q189. The N142 side chain adopts a conformation to cap on the MPI18 opal side chain and the Q189 side chain amide forms a hydrogen bond with the *N*-terminal carbamate carbonyl oxygen atom. MPI19 is structurally similar to MPI13 except an additional methyl group at the P2 β-carbon position. As shown in Fig. 3H, MPI19 interacts with M^{Pro} similar to MPI13 except that the N142 side chain in M^{Pro}-MPI19 adopts a conformation to cap the M^{Pro} P1 binding pocket for the MPI19 P1 opal residue. Except a cyclopropyl group at the P3 position, MPI20 is structurally similar to MPI11. As shown in Fig. 3I, MPI20 interacts with M^{Pro} similar to MPI11. A water molecule bridges the interaction between the Q189 side chain amide and the MPI20 P2 α-amine. The N142 side chain caps the M^{Pro} P1 binding pocket. In M^{Pro}-MPI20, electron density around residues 45–50 is too weak to model these residues, indicating that this loop region adopts a highly flexible conformation. The same region shows weak electron density in M^{Pro}-MPI16, M^{Pro}-MPI18 and M^{Pro}-MPI19.

MPI21 has α-methyl-valine at its P3 position. Compared to MPI11, the additional P3 α-methyl group pushed the *N*-terminal carbamate of MPI21 to adopt an orientation that rotates about 90° from the one shown in M^{Pro}-MPI11 (Fig. 3J). Although the Q189 side chain amide is within the hydrogen bond distance to the MPI21 *N*-terminal carbamate carbonyl oxygen atom, the geometry is not right. Compared to other inhibitors that have a regular L-amino acid at their P3 position, this different orientation at the *N*-terminal carbamate in MPI21 apparently leaves space for the Q189 side chain to move deeper toward the M^{Pro} active site. In M^{Pro}-MPI21, the N142 side chain adopts a conformation similar to the one shown in M^{Pro}-MPI11. MPI22 is structurally similar to MPI21 but contains dimethylglycine at its P3 position. The M^{Pro}-MPI22 structure at the M^{Pro} active site is very similar to M^{Pro}-MPI21. The pro-*S* methyl group at the MPI22 P3 residue pushes the *N*-terminal carbamate to adopt a conformation that positions its carbamate carbonyl oxygen away from forming a hydrogen bond with the Q189 side chain amide (Fig. 3K). As same as in M^{Pro}-MPI21, this new orientation at the *N*-terminal carbamate leaves space for the Q189 side chain to move deeper toward the M^{Pro} active site. MPI23 has a cyclopropyl backbone at its P3 position. Similar to MPI21 and MPI22, this cyclopropyl group pushes the *N*-terminal carbamate to adopt a conformation that positions the carbamate carbonyl oxygen atom away from forming a hydrogen bond with the Q189 side chain amide through the rotating extend of the carbamate is not as much as in MPI21 and MPI22 (Figure 3L). The P2 position of MPI23 is β-cyclohexyl-alanine. The cyclohexyl group has defined, strong density that indicates a chair conformation. The cyclohexyl group aligns parallelly with respect to the H41 side chain, making two C–H groups from the cyclohexyl group directly interact with the π orbital of the H41 side chain. Compared to MPI11, the P2 residue of MPI23 is larger and pushes the Q189-containing loop to move slightly away from the active site. MPI24 has a structure similar to MPI13. It has a cyclopropyl group compared to an isopropyl group in MPI13 at the P3 β-carbon. The interactions between MPI24 and M^{Pro} are also similar to that between MPI13 and M^{Pro} (Figure 3M). In M^{Pro}-MPI24, The N142 side chain caps the M^{Pro} P1 binding pocket and the Q189 side chain amide forms a hydrogen bond with the MPI24 P2 α-amine. In M^{Pro}-MPI21, M^{Pro}-MPI22, M^{Pro}-MPI23, and M^{Pro}-MPI24, the M49-containing loop has weak electron density that leads to structures of certain residues in M^{Pro}-MPI21 and M^{Pro}-MPI22 not able to be refined.

MPI25 is a MPI8 derivative. Its interactions with M^{Pro} involve most hydrogen bonds that exist in the M^{Pro}-MPI11 structure (Figure 3N). In M^{Pro}-MPI25, the N142 side chain points away from the position that can cap the M^{Pro} P1 binding pocket and the Q189 side chain amide interacts with the MPI25 P3 side chain oxygen through two water-bridged hydrogen bonds. Since the electron density around the *N*-terminal group is weak, the chloride position cannot be unambiguously assigned but it is with high confidence that it interacts with the P168 side chain. In M^{Pro}-MPI25, The M49-containing loop also has relatively weak electron density so that the M49 side chain conformation cannot be unambiguously assigned either. The *O*-*tert*-butyl group in the P3 residue has strong electron density that was used to unambiguously refine its structure that interacts with the P168 and E166 side chains. MPI26 is structurally different from MPI25 only at the P2 residue. As shown in Figure 3O, the binding model of MPI26 at the M^{Pro} active site is very similar to MPI25. Visible differences are at M^{Pro} residues N142 and Q189. In M^{Pro}-MPI26, the N142 side chain adopts a conformation that caps the M^{Pro} P1 binding pocket and the Q189 side chain amide forms hydrogen bonds separately with the MPI26 P2 α-amine and the *N*-terminal carbamate carbonyl oxygen. The electron density around residues 45–50 is also too weak to be used to refine their structures. The electron

density around the P2 leucine β-isopropyl group allows only one methyl group can be clearly refined, indicating that the P2 leucine β-isopropyl group may adopt different conformations. MPI27 is structurally different from MPI25 only at its P3 position that is valine. As shown in Figure 3P, MPI27 interacts with M^{Pro} similar to MPI25. In M^{Pro}-MPI27, the P3 valine side chain packs on top of the E166 side chain to form van der Waals interactions. The Q189 side chain amide forms a hydrogen bond with the MPI27 P2 α-amine. Unlike all other inhibitors, MPI28 has a *N*-terminal indole-2-carbonyl protection group. Its interactions with M^{Pro} shown in Figure 3Q are similar to that in M^{Pro}-MPI11. The Q189 side chain amide forms a hydrogen bond with the *N*-terminal amide oxygen. As in most other M^{Pro}-inhibitor structures, the electron density at the *N*-terminal group is too weak to refine its accurate structure. Like in M^{Pro}-MPI26, the electron density at the P2 leucine β-isopropyl group allows the refinement of only one methyl group, indicating flexible binding of this group at the M^{Pro} active site. In M^{Pro}-MPI28, the electron density around M^{Pro} residues 46–50 is too weak to be used to refine their structures. Although some of M^{Pro}-inhibitor complexes have refined structures for residues 45–50, all of them have relatively weaker electron density around these residues than other parts of M^{Pro}, indicating that the M49-containing loop is flexible after an inhibitor binds to the M^{Pro} active site.

2.4. Characterizations of cellular M^{Pro} inhibition potency of MPI11-28

M^{Pro} is acutely toxic to a human cell host. Using this unique characteristic, we developed a cell-based analysis to characterize cellular M^{Pro} inhibition potency for compounds [31]. A similar assay was also used by others to analyze cellular potency of M^{Pro} inhibitors [33,34]. In this assay, a compound with cellular potency inhibits cellular toxicity from the expression of an M^{Pro}-eGFP fusion protein, leading to enhanced overall expression of M^{Pro}-eGFP that can be characterized by flow cytometry. This assay is more advantageous over an antiviral assay in analyzing the cellular M^{Pro} inhibition ability of a compound since it may inhibit host proteases such as TMPRSS2, furin, and cathepsin L that are critical for SARS-CoV-2 infection to provide false positive cellular potency results for M^{Pro} inhibition [35–37]. We used this method to characterize a number of investigational M^{Pro} inhibitors. Our study showed some inhibitors that have demonstrated antiviral potency do not inhibit M^{Pro} directly in a human cell host, indicating different mechanisms for these compounds to achieve antiviral potency [31]. Other advantages of using this assay include quickly priming potent inhibitors for their antiviral assays by bypassing cellular permeability and stability tests and avoiding time-consuming and more complicated antiviral tests that involve the use of a biosafety level 3 facility for compounds with low cellular potency. We adopted this assay to characterize MPI11-28. All inhibitors were tested up to 10 μM in their inhibition of M^{Pro}-eGFP that was transiently expressed in human 293T cells. Overall cellular eGFP fluorescence was plotted against the inhibition concentration to obtain their EC_{50} values. Results are presented in Fig. 4 and Table 1. As shown in Fig. 4A, MPI11-14 exhibited minimal cellular potency to inhibit M^{Pro} in 293T cells, which is in significant contrast to their very high *in vitro* enzyme inhibition potency. Since their inhibition curves do not reach a plateau, their EC_{50} values are estimated as > 2 μM. MPI16 and MPI17 are the two most potent inhibitors among MPI11-28 on cellular potency with determined EC_{50} values as 56 nM and 97 nM, respectively (Fig. 4B). In comparison to MPI16 and MPI17, MPI18 and MPI19 have weaker cellular potency with determined EC_{50} values as 860 nM and 1500 nM, respectively. MPI20-23 all have weak cellular potency (Fig. 4C). MPI22 and MPI23 showed very low inhibition of M^{Pro}-eGFP in 293T cells. At 10 μM for these two compounds, M^{Pro}-eGFP expression was lower than half of the plateau level of M^{Pro}-eGFP that was observed for MPI16-19. For these four inhibitors, their EC_{50} values are estimated as > 2 μM for MPI20 and MPI21 and > 10 μM for MPI22 and MPI23. Among MPI24-28 (Fig. 4D), MPI25-27 exhibited high cellular potency with EC_{50} values as 140 nM, 230 nM, and 630 nM respectively. On contrary to their high *in vitro* enzyme inhibition potency, MPI24 and MPI28 have very weak cellular potency with estimated EC_{50} values as > 2 μM and >10 μM, respectively. Two reported M^{Pro} inhibitors nirmatrelvir [29] and GC376 [7] were tested for *in cellulo* M^{Pro} inhibition potency. Nirmatrelvir has a determined *in cellulo* EC_{50} value as 3.4 μM [38], and GC376 shows a *in cellulo* EC_{50} value of >2 μM

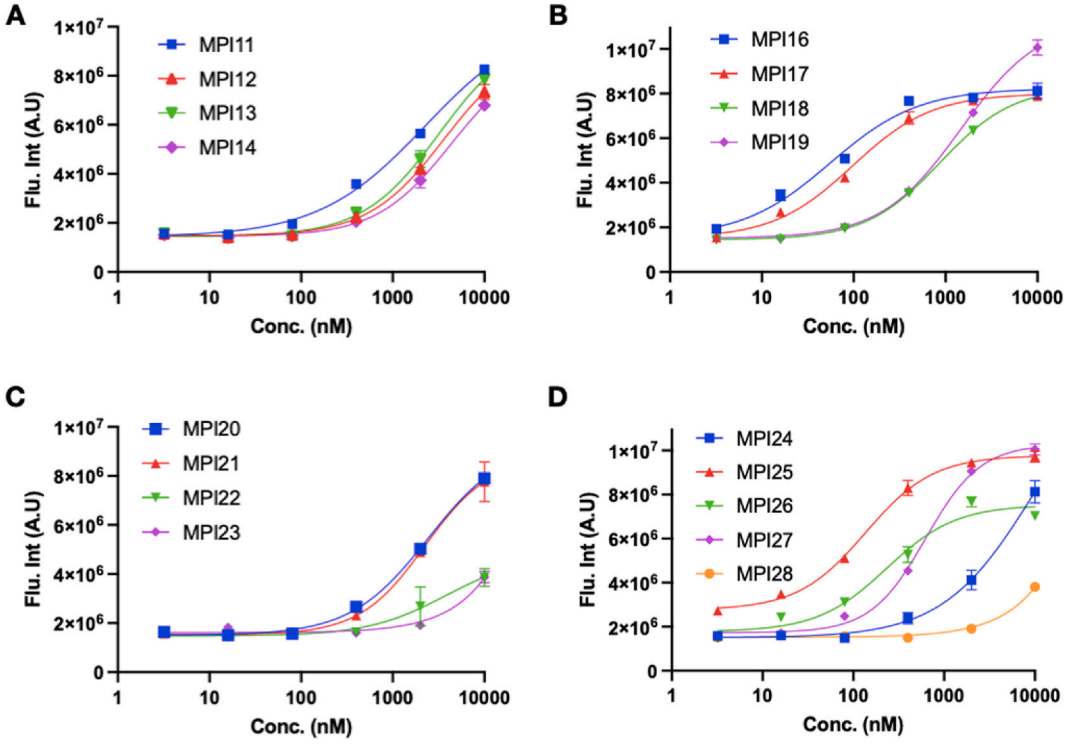

Fig. 4. Cellular potency of MPI11-28 in their inhibition of M^{Pro} to drive host 293T cell survival and overall M^{Pro}-eGFP expression.

(Table 1) [31]. Their cellular potency are weaker compared to MPI16, MPI17, MPI25, and MPI26.

2.5. Characterizations of antiviral potency of six selected inhibitors on three SARS-CoV-2 variants

Four most cellularly potent inhibitors MPI16, MPI17, MPI25, and MPI26 that contain a P3 *O-tert*-butyl-threonine and two mildly cellularly potent inhibitors MPI18 and MPI27 that don't contain a P3 *O-tert*-butyl-threonine were analyzed on their antiviral potency against three SARS-CoV-2 variants including USA-WA1/2020, Beta and Delta (Fig. 5). We conducted plaque reduction neutralization tests in Vero E6 cells for all inhibitors. We infected Vero E6 cells by virus in the presence of an inhibitor at various concentrations for three days and then quantified viral plaque reduction. As presented in the attached figure and table, all four inhibitors that contain a P3 *O-tert*-butyl-threonine showed high antiviral potency with determined EC_{50} values around 1 μM and MPI18 and MPI27 that don't have a P3 *O-tert*-butyl-threonine showed only moderate antiviral potency. It should be noted that MPI5 containing a P3 valine showed mild cellular M^{Pro} inhibition potency but potent antiviral activity [13,31]. Its antiviral activity may not only come from the inhibition of M^{Pro} but also other mechanisms.

2.6. Cytotoxicity of MPI8, MPI16, MPI17, MPI18, MPI25, MPI26 and MPI27

We characterized cytotoxicity for these seven compounds in 293T cells using the MTT assay [39]. Cytotoxicity curves of these inhibitors are shown in Supplementary Fig. S2. Their determined CC_{50} values are 109.2, >200, >200, >200, 130, 182.9 and 114.0 μM for MPI8, MPI16, MPI17, MPI18, MPI25, MPI26 and MPI27, respectively (Table 1). In term of selectivity index (CC_{50}/antiviral EC_{50}), MPI8, MPI16, MPI17, and MPI18 are around or above 200.

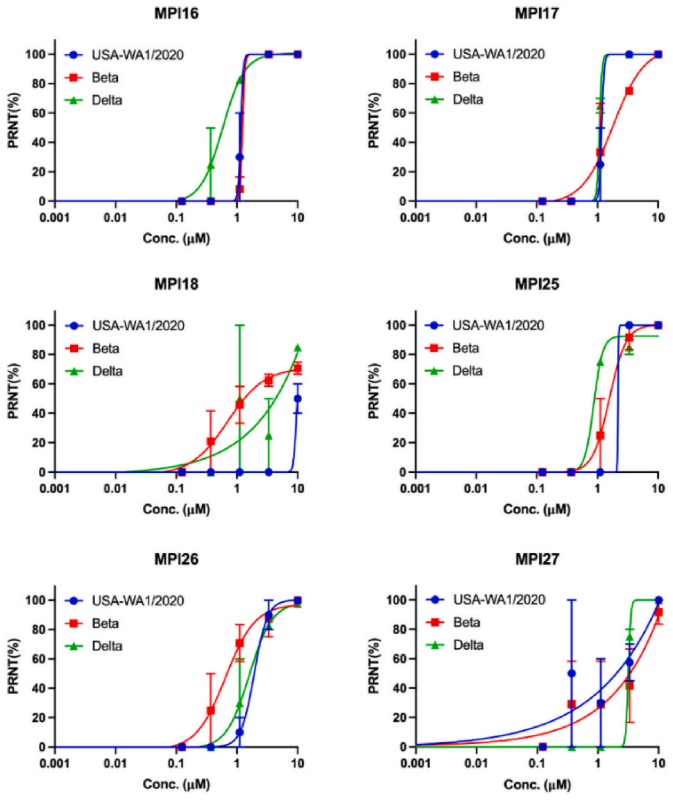

Fig. 5. Plaque reduction neutralization tests (PRNTs) of MPI16-18 and MPI25-27 on their inhibition of three SARS-CoV-2 strains USA-WA1/2020, Beta and Delta in Vero E6 cells. Two repeats were conducted for each concentration.

3. Discussion

There are 11 unique proteolytic sites in pp1a and pp1b that are hydrolyzed by M^{Pro}. Glutamine is a strictly required residue at the P1 site for all 11 sites. Due to this strict requirement and medicinal chemistry information learnt from the same function enzyme in SARS-CoV, most peptidyl inhibitors that have been developed for M^{Pro} have maintained a β-(S-2-oxopyrrolidin-3-yl)-alanine analog at the P1 site for improved potency. In our design, we keep opal at this site for all inhibitors. Our crystallography results show a well-shaped opal side chain in all M^{Pro}-inhibitor complexes that fits neatly in the P1 binding pocket of the enzyme. Since opal is optimized for this site, there is small chemical space to manipulate its side chain for improved binding. In all determined structures, the side chain of N142 adopts different conformations that do not necessarily interact with the opal oxopyrrolidine ring. It may be possible to modify the opal oxopyrrolidine ring to introduce interactions such as hydrogen bond(s) with the N142 side chain for improved binding. Among all 11 M^{Pro}-targeted proteolytic sites, 9 have a P2 leucine, 1 has a P2 phenylalanine, and 1 has a P2 valine. The enzyme has an apparent preference for a P2 leucine in its substrates. A comparison of *in vitro* enzyme inhibition potency for all MPIs that we have developed also reveals that M^{Pro} prefers a P2 residue with a similar size as leucine in a peptidyl inhibitor for favorable binding. Converting the isopropyl group at the β-carbon of the P2 residue to cyclopropyl and 2-furanyl improves the enzyme inhibition kinetics. Although changing the P2 leucine in an inhibitor to a larger residue such as phenylalanine and β-cyclohexylalanine diminishes *in vitro* M^{Pro} inhibition potency, the level is not significant. It is interesting to see that a β-isoprenyl group at the P2 residue has no fixed conformation but a cyclopropyl group at the same position has a defined conformation in crystal structures. Since inhibitors with a β-cyclopropyl group at the P2 residue have typically high *in vitro* enzyme inhibition potency, it is possible that adding an additional group such as methyl to the β-carbon of a P2 β-cyclopropyl-alanine will lead to better inhibitors. In the crystal structure of M^{Pro}-MPI14, the P2 side chain of MPI14 forms a π-π stacking interaction. This π-π stacking interaction likely contributes to the high *in vitro* enzymatic inhibition potency of MPI14. Although MPI15 is not soluble, it is expected to have high *in vitro* enzymatic inhibition potency as well due to a similar -π stacking interaction that can be formed between MPI15 and M^{Pro}. Other five-membered rings that contain one or more heteroatoms at the P2 β-carbon may also lead to high *in vitro* enzymatic inhibition potency since a similar π-π stacking interaction can be formed between them and M^{Pro}. In most of our determined M^{Pro}-inhibitor complexes, we noticed that the M49-containing loop of M^{Pro} has weak electron density, indicating that this loop adopts a flexible structure. Since this loop caps the M^{Pro} P2 binding pocket, this flexibility will potentially allow peptide inhibitors with a P2 residue larger than all moieties that have been tested in our inhibitors at this site to be tolerated by M^{Pro}. This probability needs to be explored.

M^{Pro} shows almost no preference toward the P3 residue in its targeted proteolytic sites in pp1a and pp1b. We explored a variety of chemical variants at this site including dialkyl glycines and 1-aminocyclopropane-1-carboxylate that have no α-proton. Although M^{Pro} displays a clear preference for a P3 valine, other substituents at this site are well tolerated. For most inhibitors, their P3 residues can be well refined. Given the diverse structures of tolerable chemical compositions at this site, D-amino acids might be introduced at this site for the development of novel M^{Pro} inhibitors as well. This will need to be explored further. One interesting observation is that α,α-disubstituted glycines at the P3 position push their adjacent *N*-terminal carbamate carbonyl group to adopt an orientation rotating about 90° away from a position that has been observed in M^{Pro}-inhibitor structures into the M^{Pro} active site. It will be interesting to see whether this observation can be applied to optimize existing M^{Pro} inhibitors including nirmatrelvir to achieve

better antiviral potency. All our crystal structures show weak electron density around the *N*-terminal group indicating its weak binding to the enzyme. Adding an *m*-chloride to the *N*-terminal CBZ group also leads to significant decrease in *in vitro* enzyme inhibition potency. So far, our studies indicate that both CBZ and indole-2-carboxyl are not optimal chemical groups for interactions with M^{Pro}. Some smaller groups need to be explored at this site. One example will be trifluoroacetamide as seen in nirmatrelvir.

Although most inhibitors we have developed in this study have high *in vitro* enzyme inhibition potency and two inhibitors have IC_{50} values reaching the characterization limit, just a few inhibitors show cellular potency to inhibit M^{Pro} in 293T cells. Inhibitors that have a P3 *O-tert*-butyl-threonine all show strong cellular potency. All other P3 substituents lead to relatively weaker cellular potency, although MPI5, MPI18, and MPI27 showed mild cellular potency. Many factors may contribute to this phenomenon. Since all MPIs are peptidyl inhibitors, a small or native P3 residue might be prone to proteolytic degradation by host proteases leading to low cellular potency. This is partially supported by characterizable cellular potency for MPI18-19 that have a P3 β-*tert*-butyl-alanine. It is also likely that a P3 *O-tert*-butyl-threonine introduces more favorable cellular permeability than other P3 substituents into an M^{Pro} inhibitor. This aspect needs to be further investigated. MPI21-23 that have a P3 dialkylglycine are expected to be more resistant to proteolytic digestion by human proteases than other MPIs. Their low cellular potency might be due to low cellular permeability. Based on cellular potency of MPIs, we can also derive that an *N*-terminal CBZ group works better than the other two groups that have been tested at this site and a P2 β-cyclohexylalanine favors high cellular potency as well.

In terms of antiviral potency, results for six tested compounds agree well with their cellular potency, supporting the notion that the inhibition of M^{Pro} in infected cells is enough to achieve the prevention of viral replication. It should be noted that 293T cells were used in the cellular assay and Vero E6 cells were used in the antiviral assay. Different cell lines may have different enzymes which may contribute to different metabolism of inhibitors, leading to the discrepancy between cellular M^{Pro} inhibition potency and antiviral potency. Six tested inhibitors also exhibited relatively low cytotoxicity. With this level of selectivity, potential achievement of their use in containing SARS-CoV-2 in COVID-19 patients is possible. However, all inhibitors have an aldehyde functionality that is potentially metabolically unstable. Exploration of other warheads such as nitrile that was used in nirmatrelvir might potentially solve both metabolic and cytotoxicity concerns.

Author contributions

H. Ji, S. Xu and W. R. Liu conceived the project and directed the study; Y. Ma, Y. R. Alugubelli, X. R. Ma, and K. Khatua synthesized and characterized chemically all inhibitors; K. S. Yang, E. C. Vatansever and G. Yu characterized *in vitro* IC_{50} values of all synthesized inhibitors; Z. Z. Geng and C.-C. Cho characterized cellular EC_{50} values of all synthesized inhibitors; K. S. Yang, L. R. Blankenship, B. Sankaran, and P. Li determined all protein crystal structures; N. Shaabani and R. Allen characterized antiviral EC_{50} values for selected inhibitors; J. Xiao characterized CC_{50} for selected inhibitors; H. Ji, S. Xu and W. R. Liu wrote the manuscript.

Declaration of competing interest

The authors declare that they have no known competing financial interests or personal relationships that could have appeared to influence the work reported in this paper.

Data availability

Data will be made available on request.

Acknowledgement

This work was supported by Welch Foundation (grant A-1715), National Institutes of Health (Grants R21AI164088 and R21EB032983), TAMU COS Strategic Transformative Research Program, and Texas A&M X Grants. The ALS-ENABLE beam-lines are supported in part by the National Institutes of Health, National Institute of General Medical Sciences, grant P30 GM124169-01 and the Howard Hughes Medical Institute. The Advanced Light Source is a Department of Energy Office of Science User Facility under Contract No. DE-AC02-05CH11231.

Appendix A. Supplementary data

Supplementary data to this article can be found online at https://doi.org/10.1016/j.ejmech.2022.114570.

References

[1] J. Lan, J. Ge, J. Yu, S. Shan, H. Zhou, S. Fan, Q. Zhang, X. Shi, Q. Wang, L. Zhang, X. Wang, Structure of the SARS-CoV-2 spike receptor-binding domain bound to the ACE2 receptor, Nature 581 (7807) (2020) 215–220.
[2] R. Yan, Y. Zhang, Y. Li, L. Xia, Y. Guo, Q. Zhou, Structural basis for the recognition of SARS-CoV-2 by full-length human ACE2, Science 367 (6485) (2020) 1444–1448.
[3] D. Kim, J.Y. Lee, J.S. Yang, J.W. Kim, V.N. Kim, H. Chang, The architecture of SARS-CoV-2 transcriptome, Cell 181 (4) (2020) 914–921 e10.
[4] P. Zhou, X.L. Yang, X.G. Wang, B. Hu, L. Zhang, W. Zhang, H.R. Si, Y. Zhu, B. Li, C. L. Huang, H.D. Chen, J. Chen, Y. Luo, H. Guo, R.D. Jiang, M.Q. Liu, Y. Chen, X. R. Shen, X. Wang, X.S. Zheng, K. Zhao, Q.J. Chen, F. Deng, L.L. Liu, B. Yan, F. X. Zhan, Y.Y. Wang, G.F. Xiao, Z.L. Shi, A pneumonia outbreak associated with a new coronavirus of probable bat origin, Nature 579 (7798) (2020) 270–273.
[5] J.S. Morse, T. Lalonde, S. Xu, W.R. Liu, Learning from the past: possible urgent prevention and treatment options for severe acute respiratory infections caused by 2019-nCoV, Chembiochem 21 (5) (2020) 730–738.
[6] W. Dai, B. Zhang, X.M. Jiang, H. Su, J. Li, Y. Zhao, X. Xie, Z. Jin, J. Peng, F. Liu, C. Li, Y. Li, F. Bai, H. Wang, X. Cheng, X. Cen, S. Hu, X. Yang, J. Wang, X. Liu, G. Xiao, H. Jiang, Z. Rao, L.K. Zhang, Y. Xu, H. Yang, H. Liu, Structure-based design of antiviral drug candidates targeting the SARS-CoV-2 main protease, Science 368 (6497) (2020) 1331–1335.
[7] L. Fu, F. Ye, Y. Feng, F. Yu, Q. Wang, Y. Wu, C. Zhao, H. Sun, B. Huang, P. Niu, H. Song, Y. Shi, X. Li, W. Tan, J. Qi, G.F. Gao, Both Boceprevir and GC376 efficaciously inhibit SARS-CoV-2 by targeting its main protease, Nat. Commun. 11 (1) (2020) 4417.
[8] W. Dai, D. Jochmans, H. Xie, H. Yang, J. Li, H. Su, D. Chang, J. Wang, J. Peng, L. Zhu, Y. Nian, R. Hilgenfeld, H. Jiang, K. Chen, L. Zhang, Y. Xu, J. Neyts, H. Liu, Design, synthesis, and biological evaluation of peptidomimetic aldehydes as broad-spectrum inhibitors against enterovirus and SARS-CoV-2, J. Med. Chem. (2021), https://doi.org/10.1021/acs.jmedchem.0c02258.
[9] J. Qiao, Y.S. Li, R. Zeng, F.L. Liu, R.H. Luo, C. Huang, Y.F. Wang, J. Zhang, B. Quan, C. Shen, X. Mao, X. Liu, W. Sun, W. Yang, X. Ni, K. Wang, L. Xu, Z.L. Duan, Q. C. Zou, H.L. Zhang, W. Qu, Y.H. Long, M.H. Li, R.C. Yang, X. Liu, J. You, Y. Zhou, R. Yao, W.P. Li, J.M. Liu, P. Chen, Y. Liu, G.F. Lin, X. Yang, J. Zou, L. Li, Y. Hu, G. W. Lu, W.M. Li, Y.Q. Wei, Y.T. Zheng, J. Lei, S. Yang, SARS-CoV-2 M(pro) inhibitors with antiviral activity in a transgenic mouse model, Science 371 (6536) (2021) 1374–1378.
[10] R.L. Hoffman, R.S. Kania, M.A. Brothers, J.F. Davies, R.A. Ferre, K.S. Gajiwala, M. He, R.J. Hogan, K. Kozminski, L.Y. Li, J.W. Lockner, J. Lou, M.T. Marra, L. J. Mitchell Jr., B.W. Murray, J.A. Nieman, S. Noell, S.P. Planken, T. Rowe, K. Ryan, G.J. Smith 3rd, J.E. Solowiej, C.M. Steppan, B. Taggart, Discovery of Ketone-based covalent inhibitors of coronavirus 3CL proteases for the potential therapeutic treatment of COVID-19, J. Med. Chem. 63 (21) (2020) 12725–12747.
[11] C. Ma, M.D. Sacco, B. Hurst, J.A. Townsend, Y. Hu, T. Szeto, X. Zhang, B. Tarbet, M.T. Marty, Y. Chen, J. Wang, Boceprevir, GC-376, and calpain inhibitors II, XII inhibit SARS-CoV-2 viral replication by targeting the viral main protease, Cell Res. 30 (8) (2020) 678–692.
[12] M.D. Sacco, C. Ma, P. Lagarias, A. Gao, J.A. Townsend, X. Meng, P. Dube, X. Zhang, Y. Hu, N. Kitamura, B. Hurst, B. Tarbet, M.T. Marty, A. Kolocouris, Y. Xiang, Y. Chen, J. Wang, Structure and inhibition of the SARS-CoV-2 main protease reveal strategy for developing dual inhibitors against M(pro) and cathepsin L, Sci. Adv. 6 (50) (2020), eabe0751.
[13] K.S. Yang, X.R. Ma, Y. Ma, Y.R. Alugubelli, D.A. Scott, E.C. Vatansever, A. K. Drelich, B. Sankaran, Z.Z. Geng, L.R. Blankenship, H.E. Ward, Y.J. Sheng, J. C. Hsu, K.C. Kratch, B. Zhao, H.S. Hayatshahi, J. Liu, P. Li, C.A. Fierke, C.K. Tseng, S. Xu, W.R. Liu, A quick route to multiple highly potent SARS-CoV-2 main protease inhibitors, ChemMedChem 16 (6) (2021) 942–948.
[14] X.R. Ma, Y.R. Alugubelli, Y. Ma, E.C. Vatansever, D.A. Scott, Y. Qiao, G. Yu, S. Xu, W.R. Liu, MPI8 is potent against SARS-CoV-2 by inhibiting dually and selectively the SARS-CoV-2 main protease and the host cathepsin L, ChemMedChem 17 (1) (2022), e202100456.
[15] A. Douangamath, D. Fearon, P. Gehrtz, T. Krojer, P. Lukacik, C.D. Owen, E. Resnick, C. Strain-Damerell, A. Aimon, P. Abranyi-Balogh, J. Brandao-Neto, A. Carbery, G. Davison, A. Dias, T.D. Downes, L. Dunnett, M. Fairhead, J.D. Firth,

S.P. Jones, A. Keeley, G.M. Keseru, H.F. Klein, M.P. Martin, M.E.M. Noble, P. O'Brien, A. Powell, R.N. Reddi, R. Skyner, M. Snee, M.J. Waring, C. Wild, N. London, F. von Delft, M.A. Walsh, Crystallographic and electrophilic fragment screening of the SARS-CoV-2 main protease, Nat. Commun. 11 (1) (2020) 5047.

[16] M.M. Ghahremanpour, J. Tirado-Rives, M. Deshmukh, J.A. Ippolito, C.H. Zhang, I. Cabeza de Vaca, M.E. Liosi, K.S. Anderson, W.L. Jorgensen, Identification of 14 known drugs as inhibitors of the main protease of SARS-CoV-2, ACS Med. Chem. Lett. 11 (12) (2020) 2526–2533.

[17] Z. Jin, X. Du, Y. Xu, Y. Deng, M. Liu, Y. Zhao, B. Zhang, X. Li, L. Zhang, C. Peng, Y. Duan, J. Yu, L. Wang, K. Yang, F. Liu, R. Jiang, X. Yang, T. You, X. Liu, X. Yang, F. Bai, H. Liu, X. Liu, L.W. Guddat, W. Xu, G. Xiao, C. Qin, Z. Shi, H. Jiang, Z. Rao, H. Yang, Structure of M(pro) from SARS-CoV-2 and discovery of its inhibitors, Nature 582 (7811) (2020) 289–293.

[18] Z. Jin, Y. Zhao, Y. Sun, B. Zhang, H. Wang, Y. Wu, Y. Zhu, C. Zhu, T. Hu, X. Du, Y. Duan, J. Yu, X. Yang, X. Yang, K. Yang, X. Liu, L.W. Guddat, G. Xiao, L. Zhang, H. Yang, Z. Rao, Structural basis for the inhibition of SARS-CoV-2 main protease by antineoplastic drug carmofur, Nat. Struct. Mol. Biol. 27 (6) (2020) 529–532.

[19] C. Ma, Y. Hu, J.A. Townsend, P.I. Lagarias, M.T. Marty, A. Kolocouris, J. Wang, Ebselen, disulfiram, carmofur, PX-12, tideglusib, and shikonin are nonspecific promiscuous SARS-CoV-2 main protease inhibitors, ACS Pharmacol Transl Sci 3 (6) (2020) 1265–1277.

[20] A.D. Rathnayake, J. Zheng, Y. Kim, K.D. Perera, S. Mackin, D.K. Meyerholz, M. M. Kashipathy, K.P. Battaile, S. Lovell, S. Perlman, W.C. Groutas, K.O. Chang, 3C-like protease inhibitors block coronavirus replication in vitro and improve survival in MERS-CoV-infected mice, Sci. Transl. Med. 12 (557) (2020), eabc5332.

[21] W. Zhu, M. Xu, C.Z. Chen, H. Guo, M. Shen, X. Hu, P. Shinn, C. Klumpp-Thomas, S. G. Michael, W. Zheng, Identification of SARS-CoV-2 3CL protease inhibitors by a quantitative high-throughput screening, ACS Pharmacol Transl Sci 3 (5) (2020) 1008–1016.

[22] S. Gunther, P.Y.A. Reinke, Y. Fernandez-Garcia, J. Lieske, T.J. Lane, H.M. Ginn, F. H.M. Koua, C. Ehrt, W. Ewert, D. Oberthuer, O. Yefanov, S. Meier, K. Lorenzen, B. Krichel, J.D. Kopicki, L. Gelisio, W. Brehm, I. Dunkel, B. Seychell, H. Gieseler, B. Norton-Baker, B. Escudero-Perez, M. Domaracky, S. Saouane, A. Tolstikova, T. A. White, A. Hanle, M. Groessler, H. Fleckenstein, F. Trost, M. Galchenkova, Y. Gevorkov, C. Li, S. Awel, A. Peck, M. Barthelmess, F. Schlunzen, P. Lourdu Xavier, N. Werner, H. Andaleeb, N. Ullah, S. Falke, V. Srinivasan, B.A. Franca, M. Schwinzer, H. Brognaro, C. Rogers, D. Melo, J.J. Zaitseva-Doyle, J. Knoska, G. E. Pena-Murillo, A.R. Mashhour, V. Hennicke, P. Fischer, J. Hakanpaa, J. Meyer, P. Gribbon, B. Ellinger, M. Kuzikov, M. Wolf, A.R. Beccari, G. Bourenkov, D. von Stetten, G. Pompidor, I. Bento, S. Panneerselvam, I. Karpics, T.R. Schneider, M. M. Garcia-Alai, S. Niebling, C. Gunther, C. Schmidt, R. Schubert, H. Han, J. Boger, D.C.F. Monteiro, L. Zhang, X. Sun, J. Pletzer-Zelgert, J. Wollenhaupt, C.G. Feiler, M.S. Weiss, E.C. Schulz, P. Mehrabi, K. Karnicar, A. Usenik, J. Loboda, H. Tidow, A. Chari, R. Hilgenfeld, C. Uetrecht, R. Cox, A. Zaliani, T. Beck, M. Rarey, S. Gunther, D. Turk, W. Hinrichs, H.N. Chapman, A.R. Pearson, C. Betzel, A. Meents, X-ray screening identifies active site and allosteric inhibitors of SARS-CoV-2 main protease, Science 372 (6542) (2021) 642–646.

[23] S.I. Hattori, N. Higashi-Kuwata, H. Hayashi, S.R. Allu, J. Raghavaiah, H. Bulut, D. Das, B.J. Anson, E.K. Lendy, Y. Takamatsu, N. Takamune, N. Kishimoto, K. Murayama, K. Hasegawa, M. Li, D.A. Davis, E.N. Kodama, R. Yarchoan, A. Wlodawer, S. Misumi, A.D. Mesecar, A.K. Ghosh, H. Mitsuya, A small molecule compound with an indole moiety inhibits the main protease of SARS-CoV-2 and blocks virus replication, Nat. Commun. 12 (1) (2021) 668.

[24] C.J. Kuo, T.L. Chao, H.C. Kao, Y.M. Tsai, Y.K. Liu, L.H. Wang, M.C. Hsieh, S. Y. Chang, P.H. Liang, Kinetic characterization and inhibitor screening for the proteases leading to identification of drugs against SARS-CoV-2, Antimicrob. Agents Chemother. 65 (4) (2021) e02577–20.

[25] G.J. Lockbaum, A.C. Reyes, J.M. Lee, R. Tilvawala, E.A. Nalivaika, A. Ali, N. Kurt Yilmaz, P.R. Thompson, C.A. Schiffer, Crystal structure of SARS-CoV-2 main protease in complex with the non-covalent inhibitor ML188, Viruses 13 (2) (2021).

[26] D. Zaidman, P. Gehrtz, M. Filep, D. Fearon, R. Gabizon, A. Douangamath, J. Prilusky, S. Duberstein, G. Cohen, C.D. Owen, E. Resnick, C. Strain-Damerell, P. Lukacik, C. Covid-Moonshot, H. Barr, M.A. Walsh, F. von Delft, N. London, An automatic pipeline for the design of irreversible derivatives identifies a potent SARS-CoV-2 M(pro) inhibitor, Cell Chem Biol 28 (12) (2021) 1795–1806.

[27] C.H. Zhang, E.A. Stone, M. Deshmukh, J.A. Ippolito, M.M. Ghahremanpour, J. Tirado-Rives, K.A. Spasov, S. Zhang, Y. Takeo, S.N. Kudalkar, Z. Liang, F. Isaacs, B. Lindenbach, S.J. Miller, K.S. Anderson, W.L. Jorgensen, Potent noncovalent inhibitors of the main protease of SARS-CoV-2 from molecular sculpting of the drug perampanel guided by free Energy perturbation calculations, ACS Cent. Sci. 7 (3) (2021) 467–475.

[28] E.C. Vatansever, K.S. Yang, A.K. Drelich, K.C. Kratch, C.C. Cho, K.R. Kempaiah, J. C. Hsu, D.M. Mellott, S. Xu, C.K. Tseng, W.R. Liu, Bepridil is potent against SARS-CoV-2 in vitro, Proc. Natl. Acad. Sci. U. S. A. 118 (10) (2021), e2012201118.

[29] D.R. Owen, C.M.N. Allerton, A.S. Anderson, L. Aschenbrenner, M. Avery, S. Berritt, B. Boras, R.D. Cardin, A. Carlo, K.J. Coffman, A. Dantonio, L. Di, H. Eng, R. Ferre, K.S. Gajiwala, S.A. Gibson, S.E. Greasley, B.L. Hurst, E.P. Kadar, A.S. Kalgutkar, J. C. Lee, J. Lee, W. Liu, S.W. Mason, S. Noell, J.J. Novak, R.S. Obach, K. Ogilvie, N. C. Patel, M. Pettersson, D.K. Rai, M.R. Reese, M.F. Sammons, J.G. Sathish, R.S. P. Singh, C.M. Steppan, A.E. Stewart, J.B. Tuttle, L. Updyke, P.R. Verhoest, L. Wei, Q. Yang, Y. Zhu, An oral SARS-CoV-2 M(pro) inhibitor clinical candidate for the treatment of COVID-19, Science 374 (6575) (2021) 1586–1593.

[30] K.S. Yang, S.Z. Leeuwon, S. Xu, W.R. Liu, Evolutionary and structural insights about potential SARS-CoV-2 evasion of nirmatrelvir, J. Med. Chem. (2022), https://doi.org/10.1021/acs.jmedchem.2c00404.

[31] W. Cao, C.-C.D. Cho, Z.Z. Geng, N. Shaabani, X.R. Ma, E.C. Vatansever, Y. R. Alugubelli, Y. Ma, S.P. Chaki, W.H. Ellenburg, K.S. Yang, Y. Qiao, R. Allen, B. W. Neuman, H. Ji, S. Xu, W.R. Liu, Evaluation of SARS-CoV-2 main protease inhibitors using a novel cell-based assay, ACS Cent. Sci. 8 (2) (2022) 192–204.

[32] C. Ma, Z. Xia, M.D. Sacco, Y. Hu, J.A. Townsend, X. Meng, J. Choza, H. Tan, J. Jang, M.V. Gongora, X. Zhang, F. Zhang, Y. Xiang, M.T. Marty, Y. Chen, J. Wang, Discovery of di- and trihaloacetamides as covalent SARS-CoV-2 main protease inhibitors with high target specificity, J. Am. Chem. Soc. 143 (49) (2021) 20697–20709.

[33] S.J. Resnick, S. Iketani, S.J. Hong, A. Zask, H. Liu, S. Kim, S. Melore, F.Y. Lin, M. S. Nair, Y. Huang, S. Lee, N.E.S. Tay, T. Rovis, H.W. Yang, L. Xing, B.R. Stockwell, D.D. Ho, A. Chavez, Inhibitors of coronavirus 3CL proteases protect cells from protease-mediated cytotoxicity, J. Virol. 95 (14) (2021), e0237420.

[34] S. Iketani, F. Forouhar, H. Liu, S.J. Hong, F.Y. Lin, M.S. Nair, A. Zask, Y. Huang, L. Xing, B.R. Stockwell, A. Chavez, D.D. Ho, Lead compounds for the development of SARS-CoV-2 3CL protease inhibitors, Nat. Commun. 12 (2021) 2016.

[35] M. Hoffmann, H. Kleine-Weber, S. Schroeder, N. Kruger, T. Herrler, S. Erichsen, T. S. Schiergens, G. Herrler, N.H. Wu, A. Nitsche, M.A. Muller, C. Drosten, S. Pohlmann, SARS-CoV-2 cell entry depends on ACE2 and TMPRSS2 and is blocked by a clinically proven protease inhibitor, Cell 181 (2) (2020) 271–280, e8.

[36] Y.W. Cheng, T.L. Chao, C.L. Li, M.F. Chiu, H.C. Kao, S.H. Wang, Y.H. Pang, C. H. Lin, Y.M. Tsai, W.H. Lee, M.H. Tao, T.C. Ho, P.Y. Wu, L.T. Jang, P.J. Chen, S. Y. Chang, S.H. Yeh, Furin inhibitors block SARS-CoV-2 spike protein cleavage to suppress virus production and cytopathic effects, Cell Rep. 33 (2) (2020), 108254.

[37] M.M. Zhao, W.L. Yang, F.Y. Yang, L. Zhang, W.J. Huang, W. Hou, C.F. Fan, R. H. Jin, Y.M. Feng, Y.C. Wang, J.K. Yang, Cathepsin L plays a key role in SARS-CoV-2 infection in humans and humanized mice and is a promising target for new drug development, Signal Transduct Tar 6 (1) (2021) 134.

[38] Y.R. Alugubelli, Z.Z. Geng, K.S. Yang, N. Shaabani, K. Khatua, X.R. Ma, E. C. Vatansever, C.-C. Cho, Y. Ma, L. Blankenship, G. Yu, B. Sankaran, P. Li, R. Allen, H. Ji, S. Xu, W.R. Liu, The N-terminal carbamate is key to high cellular and antiviral potency for boceprevir-based SARS-CoV-2 main protease inhibitors, bioRxiv (2021), 2021.12.18.473330.

[39] P. Kumar, A. Nagarajan, P.D. Uchil, Analysis of cell viability by the MTT assay, Cold Spring Harb. Protoc. 2018 (6) (2018) 469–471.